JOURNAL OF SPACECRAFT AND ROCKETS
Vol. 40, No. 5, September–October 2003

Flowfield Around Spike-Tipped Bodies for High Attack Angles at Mach 4.5

P. Gnemmi,* J. Srulijes,† and K. Roussel‡
French–German Research Institute of Saint-Louis, F-68301 Saint Louis Cedex, France
and
K. Runne§
European Aeronautic Defense and Space, LFK-Lenkflugkörpersysteme GmbH, D-88039 Friedrichshafen, Germany

The requirements for the design of a new short-range high-velocity missile are both the drag reduction and the correct information acquisition for the optoelectronic sensors embedded in the hemispherical nose. High angles of attack must be studied to fulfill the maneuverability requirements of present and future missiles. A supersonic missile generates a bow shock around its blunt nose, which causes rather high surface pressure and temperature and, as a result, the development of high drag and damage of embedded sensors. The pressure and the temperature on the hemispherical nose surface can be substantially reduced if an oblique shock is generated by a forward-facing spike. Both the experiments and the computations are carried out to study the flowfield around three-dimensional blunt bodies equipped with forward-facing spikes for a large range of attack angles at a Mach number of 4.5. A blunt body, a classical disk-tip spike, a sphere-tip spike, and a biconical-tip spike are studied. The experiments involve high-pressure shock tunnel investigations using a shock tube facility. The differential interferometry technique is applied to visualize the flowfield around the different missile spike geometries. The differential interferogram pictures as well as surface pressure measurements are compared with numerical results. Numerical simulations based on steady-state three-dimensional Navier–Stokes computations are performed to predict the drag, the lift, and the pitching moment for the blunt body and for each spike-tipped missile. The computations allow one to bring out the advantages of each spike geometry in comparison to the blunt body.

Nomenclature

C_d	=	drag coefficient
C_l	=	lift coefficient
C_m	=	pitching moment coefficient
C_p	=	pressure coefficient
c_μ	=	turbulence model constant
H	=	total enthalpy, J/kg
h	=	static enthalpy, J/kg
k	=	turbulent kinetic energy, m^2/s^2
P	=	static pressure, Pa
Pr_t	=	turbulent Prandtl number
q_j	=	heat fluxes, W/m^2
S_{ui}, S_E	=	source terms, $kg/(m^2 \cdot s^2)$, $kg/(m \cdot s^3)$
t	=	time, s
u_i	=	fluid velocity in the x_i-coordinate direction, m/s
x_i	=	Cartesian coordinate, m
α	=	angle of attack, deg
δ_{ij}	=	Kronecker symbol, 1 if $i = j$ and if $i \neq j$
ε	=	dissipation of turbulent kinetic energy, m^2/s^3
λ	=	thermal conductivity, $W/(m \cdot K)$
μ	=	dynamic viscosity, $kg/(m \cdot s)$
μ_t	=	eddy viscosity, $kg/(m \cdot s)$
ρ	=	fluid density, kg/m^3
τ_{ij}	=	viscous stress tensor, N/m^2

Received 16 May 2001; revision received 13 January 2003; accepted for publication 13 January 2003.

*Senior Scientist, Aerodynamics and External Ballistics Department, 5 rue du General Cassagnou. Member AIAA.
†Senior Scientist, Shock Tube Department, 5 rue du General Cassagnou.
‡Trainee Engineer, Aerodynamics and External Ballistics Department, 5 rue du General Cassagnou.
§System Engineer, Aerodynamics, Flight Mechanics, Propulsion.

Introduction

THE specifications imposed by the European Aeronautic Defense and Space Company in Germany for the design of a new high-velocity missile of the very/short range air defense system (V/SHORADS) program are both the drag reduction and the correct information acquisition for the optoelectronic sensors embedded in the hemispherical nose.

A blunt-body missile traveling at supersonic or hypersonic speed generates a strong bow shock ahead of the blunt nose, which causes rather high pressure and temperature on the hemispherical dome surface. The high surface pressure causes the development of high drag of the body. The high flowfield temperature may cause damage to the optical and other sensing equipment typically mounted in the dome of the body nose. The pressure on the nose surface of the body can be substantially reduced if an oblique shock is generated by attaching a spike in front of the blunt body. This concept was first discussed in the 1950s as a means to reduce the heat flux and the drag on axisymmetric blunt bodies.[1–6] The pressure and the enthalpy of the fluid behind the oblique shock are lower than behind the normal shock. The spike provokes a conical separated flow zone when it has a proper length.[7] In addition, the use of a spike tip, a disk tip, for example, produces a separated region ahead of the nose cap that is a complicated merging of the spike-tip wake with the backward step-induced separation.[5] As a consequence, the blunt-body nose is shielded from the oncoming flow by the region of separation, and the spike tip reduces the drag as well as the temperature acting on the body nose and protects the surface in the case of embedded optoelectronic sensors. These sensors should be placed behind the region of separation because the interaction of the shock coming from the spike with the blunt body causes a reattachment shock with an increase of pressure and wall temperature. The effect of protection is especially desirable at high velocities to reduce the heating rate on these sensors. The optimal spike length to produce this favorable aerodynamic flow environment varies with the Mach number and the altitude of the missile at a defined angle of attack. However, when classical spikes are used, the nose drag increases drastically as the angle of attack of the body increases.[8]

The final goal of our study is to find new spike geometries and to optimize these to reach high angles of attack without losing the drag reduction effect. A bibliographical analysis[9] highlights an interesting experimental study on the feasibility of an aerospike for hypersonic missiles[10]: Drag reduction of the missile is obtained up to 14 deg of angle of attack with the use of an aerospike 3 calibers long for a Mach number of 6. The corresponding computational analysis has been carried out recently, and a modification of the $k-\varepsilon$ turbulence model is proposed to better predict the pressure distribution on the missile.[11,12]

Preliminary experiments were carried out in the French–German Research Institute of Saint-Louis (ISL) shock tube facility for the visualization of the flowfield around several spike-tipped bodies.[13] Pressure on the blunt nose surface has been measured at the same time with flush-mounted gauges giving not enough accurate information, due to the large diameter (5.5 mm) of the sensitive part of the gauges. Consistent experimental results and first computations were presented in Ref. 14.

The objective of the current paper is to perform computations of the flowfield around the tested missiles at a Mach number of 4.5 for different spike-tip geometries and for a large range of angles of attack from 0 to 45 deg. Some computation results are compared with experimental ones to validate the numerical simulation. The aim is to evaluate the benefits of each spike geometry.

The present study involves high-pressure shock tunnel investigations using the ISL shock tube facility. The differential interferometry technique is applied to visualize the flowfield around the missile to compare the flow patterns with numerical results coming from the solution of the full conservation equations. Reliable pressure measurements are carried out with transducers, allowing comparison with computations. Shock tube experiments are in progress to measure the heat flux distribution on the dome of the missiles.

Three-dimensional steady-state numerical simulations are performed, although the problem might be time dependent. In this study, we only look for the steady-state aerodynamic coefficients. However, for some steady-state computations, there is great difficulty to obtain convergence and, therefore, probably, transient computations could be better. This in turn will increase the computation costs considerably. Numerical simulations based on Navier–Stokes equations are carried out to predict the drag, the lift, and the pitching moment of each configuration. In addition, the heat flux distribution for each spike geometry is predicted but not presented yet.

Experimental Setup

Shock Tube Facility

The experiments are carried out in the ISL shock tube laboratory (Fig. 1), which has two high-pressure shock tubes (tube A and tube B) with a 100-mm inner diameter and a total length of about 30 m for both.[15–17] High-pressure shock tube B facility is used as a shock tunnel for experimentally investigating the flowfield around projectiles or missiles. For all our experiments, shock tube B is used as a shock tunnel in which the shock tube flow is expanded inside a circular parallel flow nozzle operating in the reflected mode.

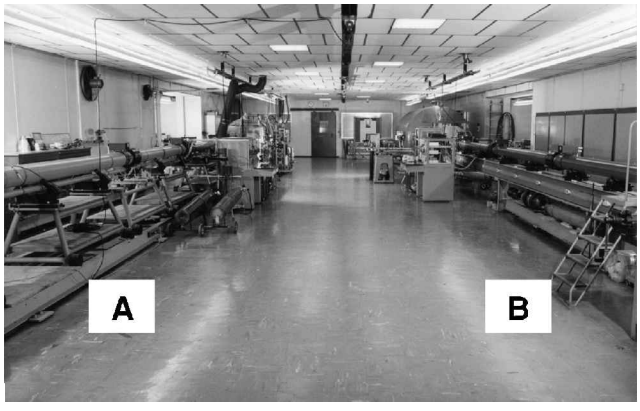

Fig. 1 ISL shock tube laboratory.

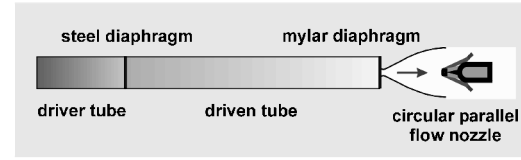

Fig. 2 Shock tunnel facility.

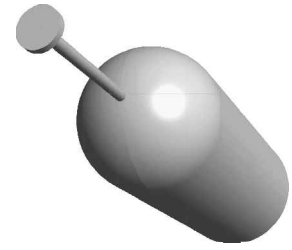

Fig. 3 V/SHORADS model with disk-tip spike.

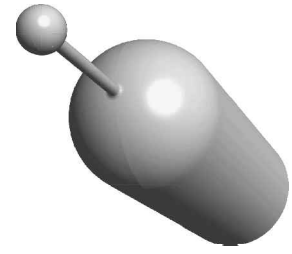

Fig. 4 V/SHORADS model with sphere-tip spike.

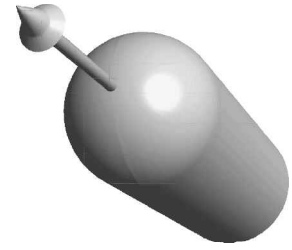

Fig. 5 V/SHORADS model with biconical-tip spike.

The shock tunnel consists of a high-pressure driver tube, a driven tube, and a circular parallel flow nozzle attached at the end of the shock tube, as shown in principle in Fig. 2. A steel diaphragm separates the hydrogen- or helium-filled driver tube from the air-filled driven tube. A Mylar diaphragm isolates the driven tube from the nozzle. The driver gas pressure reaches up to 60 MPa, and the initial driven gas pressure varies between 100 and 600 kPa.

After the diaphragm bursts, a shock wave is generated inside the driven tube and moves toward the end of the shock tube. At the nozzle throat, the incident shock wave is reflected, generating a quiescent high-pressure and high-temperature gas volume in front of the nozzle. This gas is expanded and accelerated inside the nozzle in such a way that the desired flight conditions are present at the nozzle exit.

Atmospheric flight conditions can be duplicated in the ISL shock tube facility, ranging from ground level up to more than 10 km in altitude. To reproduce flight conditions in the test facility, the body is fixed in a test chamber at the front of the nozzle and the airflow is accelerated to the desired pressure, temperature, and flight velocity.

Missile Model

In the study, the flowfield around missile models of 70-mm diam is investigated. Different models have been studied in the preliminary experiments.[13,14] In the current paper, we focus our attention on four models: the basic one is a 2.5-caliber-long hemisphere–cylinder body. The second model has a disk-tip spike added in front of the basic model (Fig. 3). The third one has a sphere tip instead of a disk tip (Fig. 4). Based on the dimensions of these spikes and inspired by the work of Shoemaker,[18] a fourth model has a biconical-tip spike. That spike has a 20–40-deg bicone at the tip (Fig. 5). Note that this

biconical tip is not optimized for our flow conditions. The diameter of the disk tip, the sphere tip, and the biconical tip is 17.5 mm.

The influence of the spike length was experimentally studied for the imposed flight conditions for 0-deg of angle of attack (AOA).[13] The results of that study suggest that the most interesting length to be studied corresponds to a spike length of about one missile caliber: The spike length is then 70 mm for the three cases.

Flow Visualization

A differential interferometer (DI) is used as a flow visualization technique[19] to gather information about the flow pattern around the missile based on the the density gradient field. Two perpendicularly polarized widened light bundles, which are separated by a prism, pass through the flowfield in parallel. They are separated by a certain distance from each other (some tenths of millimeter). The light beams are brought together by a second prism, are analyzed by a polarizer, and are focused on a drum camera by a lens system. The density changes produced in the flowfield generate different optical path lengths between the two split light bundles, giving an interference pattern on the film inside the drum camera. The DI can be adjusted to obtain fringe patterns or an infinite fringe width showing a homogeneous light intensity distribution. In this case, the pictures look like schlieren pictures. In that way, the density gradient field in the gas flow is visualized in terms of light intensity distribution shown on the interferogram pictures.

By its nature, this method, although providing integral information along the optical light path, cannot provide information in detail in three-dimensional flowfields. Thus, numerical investigations may be helpful for analyzing three-dimensional flowfields such as those suggested in the present paper.

Pressure Measurements

There are 10 pressure transducers with diameters of 2 mm that allow a measuring diameter of 1 mm mounted in the blunt-body part of the model. These transducers are located behind a hole of 0.5-mm diam and of 1.5-mm depth. In addition, a pressure gauge is mounted on the rear upper side of the cylindrical part of the model. The uncertainty of the measured pressure coefficients reported is estimated to be less than ±5%.

Numerical Simulations

Numerical simulations of the steady-state flowfield around the missile are conducted by means of the three-dimensional compressible turbulent CFX-TASCflow[20] code.

Governing Equations

The computational fluid dynamics (CFD) code models the conservation equations of mass, momentum, and energy in terms of the dependent variables (velocity, pressure, and enthalpy): They are time dependent in a turbulent flow. These quantities are decomposed into a mean component and a fluctuating one, and the original conservation equations are converted to an averaged form. For compressible flows, the mean form of the equations is obtained through a time-averaging process, usually called Reynolds-stress averaging, and a technique of mass-averaging, also called Favre averaging (see Refs. 20 and 21). The original equations for the conservation of mass, momentum, and energy may be expressed in tensor form (with the Einstein summation convention) in terms of time- and Favre-averaged quantities:

$$\frac{\partial \bar{\rho}}{\partial t} + \frac{\partial}{\partial x_j}(\bar{\rho}\tilde{u}_j) = 0 \tag{1}$$

$$\frac{\partial}{\partial t}(\bar{\rho}\tilde{u}_i) + \frac{\partial}{\partial x_j}(\bar{\rho}\tilde{u}_j\tilde{u}_i) = -\frac{\partial \bar{P}}{\partial x_i} - \frac{\partial}{\partial x_j}(\overline{\tau_{ij}} - \overline{\rho u_i'' u_j''}) + \overline{S_{ui}} \tag{2}$$

$$\frac{\partial}{\partial t}(\bar{\rho}\tilde{H}) - \frac{\partial \bar{P}}{\partial t} + \frac{\partial}{\partial x_j}(\bar{\rho}\tilde{u}_j\tilde{H}) = -\frac{\partial}{\partial x_j}(\overline{q_j} + \overline{\rho u_j'' h''}) + \frac{\partial}{\partial x_j}[\tilde{u}_i(\overline{\tau_{ij}} - \overline{\rho u_i'' u_j''}) + \overline{u_i'' \tau_{ij}''}] + \overline{S_E} \tag{3}$$

In the equations, an overbar represents the time-averaged component of a variable, a tilde indicates the Favre-averaged component of a variable, and the double prime expresses the fluctuating component coming from the mass-averaged process. Here q_j is the molecular energy transport due to heat conduction, and the S terms are additional source terms.

Equations (2) and (3) contain terms that cannot be expressed as functions of the mean flow variables: the Reynolds stresses ($\overline{\rho u_i'' u_j''}$), the turbulent energy fluxes ($\overline{\rho u_j'' h''}$), and the fluctuating viscous work term ($\overline{u_i'' \tau_{ij}''}$). These terms are related to known quantities by using a turbulence model before a close solution of the equations becomes possible. For the computations presented here, the well-known k–ε two-equation model of turbulence[21] is used to provide a link between the turbulent transport of momentum and energy and the mean flow variables and fluid properties.

Because all of the variables are mean flow quantities, it is customary to drop the symbols of time and Favre averaging. Finally, the mean conservation equations are as follows:

$$\frac{\partial \rho}{\partial t} + \frac{\partial}{\partial x_j}(\rho u_j) = 0 \tag{4}$$

$$\frac{\partial}{\partial t}(\rho u_i) + \frac{\partial}{\partial x_j}(\rho u_j u_i) = -\frac{\partial P}{\partial x_i} + \frac{\partial}{\partial x_j}\left[\mu_{\text{eff}}\left(\frac{\partial u_i}{\partial x_j} + \frac{\partial u_j}{\partial x_i}\right) - \frac{2}{3}\mu_{\text{eff}}\frac{\partial u_l}{\partial x_l}\delta_{ij}\right] + S_{ui} \tag{5}$$

$$\frac{\partial}{\partial t}(\rho H) - \frac{\partial P}{\partial t} + \frac{\partial}{\partial x_j}(\rho u_j H) = \frac{\partial}{\partial x_j}\left(\lambda\frac{\partial T}{\partial x_j} + \frac{\mu_t}{Pr_t}\frac{\partial h}{\partial x_j}\right) + \frac{\partial}{\partial x_j}\left\{u_i\left[\mu_{\text{eff}}\left(\frac{\partial u_i}{\partial x_j} + \frac{\partial u_j}{\partial x_i}\right) - \frac{2}{3}\mu_{\text{eff}}\frac{\partial u_l}{\partial x_l}\delta_{ij}\right] + \mu\frac{\partial k}{\partial x_j}\right\} + S_E \tag{6}$$

in which $\mu_{\text{eff}} = \mu_t + \mu$. The eddy viscosity μ_t is modeled as the product of a turbulence velocity scale ($\approx\sqrt{k}$) and of a turbulent length scale ($\approx k^{3/2}/\varepsilon$) as proposed by Prandtl and Komolgorov; it yields

$$\mu_t = \rho c_\mu (k^2/\varepsilon) \tag{7}$$

where ε is the dissipation rate of the turbulent kinetic energy k, μ is the dynamic viscosity of the fluid, and λ is the fluid heat conductivity. Local values of k and ε are obtained from a solution of two semi-empirical transport equations.[22]

The standard k–ε turbulence model and its Kato–Launder extension used in the present computations employ compressible wall functions (see Ref. 23) to model the viscous near-wall layer for high-speed flows. The wall function approach eliminates the necessity of numerically solving the large gradients in the thin near-wall region, thus saving valuable computer resources.

Grid Specification

The disk-spike, the sphere-spike, and the biconical-spike flowfields are numerically studied. The computation domain is reduced to one-half of the complete domain due to the symmetry of the problem. The computation is only focused on the forebody, so that the wake of the model is not meshed.

The model is located in a cylindrical volume, which is included in a prismatic volume. The boundaries of the prismatic volume are the outer limits of the computational domain. The mesh of the domain is a multiblock structured grid. The upstream boundary surface of the grid is located 1 caliber ahead of the spike tip. In the radial direction, the boundary surfaces lie at 3 calibers from the rotational axis. There are 150 × 25 × 70, 130 × 25 × 75, and 164 × 25 × 104 nodes distributed in the flowfield of the disk-spike, the sphere-spike, and the biconical-spike models, respectively (Fig. 6).

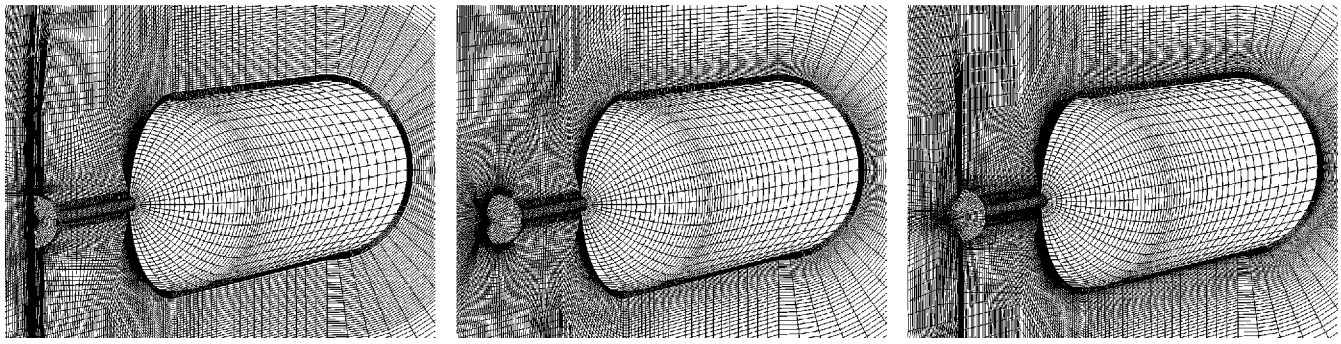

Fig. 6 Computational grids of the disk-spike, the sphere-spike, and the biconical-spike models.

The grids are built so that the mesh volumes surrounding the missiles have about the same size. The optimal performance of turbulence models is the proper resolution of the boundary layer and the correct spacing of the first point near the missile wall. The boundary layer is resolved with 10 nodes in the normal direction to the wall. The first node next to the wall is located so that $20 \leq y^+ \leq 100$ because of the use of wall functions. Finally, the distributions of nodes on the blunt-body surface and on the forebody surface of the spike-tipped missiles are identical. The distributions of nodes on the spike sting are also similar.

Boundary Conditions

The flowfield is assumed to be compressible and turbulent. Having no information about the turbulent aspect of the flow, one specifies that the turbulent kinetic energy k and its dissipation rate ε are constant along inlet regions.

The boundary conditions of the cross-flow are similar to those of the shock tube. The velocity vector, the static temperature, and the static pressure are set at the nodes of inlet regions, whereas a supersonic outlet is used for the nodes of outlet regions. A symmetry boundary condition is set in the plane of symmetry of the problem.

Solver

The CFX-TASC flow code is a finite volume method that uses four discretization schemes: the upstream differencing scheme (UDS), the mass-weighted scheme (MWS), the linear profile scheme (LPS), and a scheme that is intermediate between the last two, the modified linear profile scheme (MLPS). The UDS discretization scheme is the most robust scheme, giving a first-order prediction with a fast convergence. The LPS is numerically the most accurate discretization scheme, giving a second-order solution. A physical advection correction (PAC) can be activated for each discretization scheme to increase the accuracy of the computation.

A convergence criterion ends the computation, and a stationary converged solution of the problem is obtained. This criterion is defined as the maximum of the current dimensionless residual value for each of Eqs. (4–6). A computation is started from a constant initial flowfield by using the most robust discretization scheme and a local time step. The major computed solutions presented in this paper are converged up to 10^{-3}. They are carried out by using the MLPS discretization scheme and the PAC scheme to obtain a second-order solution.

Numerical Accuracy

A complete detailed study on supersonic projectiles and missiles has been recently carried out to examine the influence of turbulence models and grid refinements on numerical results.[24,25] Standard and renormalization group (RNG) k–ε turbulence models,[22,26] using different near-wall treatments,[23,27] have been studied. Coupled k–ε/k–ω turbulence models with different blending functions [baseline (BSL) and shear stress transport (SST) models] developed by Menter,[28] using automatic near-wall treatment,[27] have also been applied. Reynolds stress turbulence models designed by Launder et al.[29] and Speziale et al.,[30] using the same near-wall treatment as for k–ε turbulence models, have also been studied. The flowfield around different forebodies at several Mach numbers and attack angles has been computed, including flow separation in some cases. The analysis of the huge amount of computational results leads to the conclusion that the aerodynamic coefficients are slightly influenced by the choice of turbulence model based on two transport equations (k–ε and k–ε/k–ω) and by the node density in the boundary layer. The accuracy of the prediction of surface pressure, axial force, normal force, and pitching moment coefficients is estimated to be ±2%. Moreover, the computed global coefficients have been compared with experimental ones: The axial force coefficient and the derivative of the normal force coefficient are overestimated by 2 and 8%, respectively; the derivative of the pitching moment is underestimated by 5%.

The present computations are performed to mainly compare the efficiency of each spike geometry with the same accuracy. The meshes around the different spike-tipped missiles are very comparable, and the same turbulence model is applied for all computations. When the conclusion of the complete detailed study[24,25] is taken into account, the accuracy of the prediction of surface pressure, drag, lift, and pitching moment coefficients is estimated to be around ±2%.

Results and Discussion

The flowfield around the blunt body, the disk-spike, the sphere-spike, and the biconical-spike models is experimentally and numerically studied. The experiments discussed herein have been carried out for a Mach number of 4.5 and for AOA ranging from 0 to 24 deg, except for the biconical spike. The flowfield around the biconical spike is experimentally investigated at only 0-deg AOA.

The static pressure and temperature in the test chamber are 40 kPa and 240 K, respectively, corresponding to a missile altitude of about 7 km. The shock tunnel flow duration is about 4 ms. The flowfield is visualized by a series of interferogram pictures taken with a rotating drum camera. For these pictures, the flow is focused on the rotating film and eight parallax-free successive air sparks are used as light source. The time interval between the sparks is adjustable, and the start is triggered by the incident shock wave. Only one of the eight pictures, taken always at about the same time after triggering, is shown, except, for example, in the case of the sphere spike at 0-deg AOA.

Numerical simulations of the three-dimensional steady-state flowfield around the blunt body and the three spike-tipped bodies are performed for the flow conditions imposed in the experiments for AOA ranging from 0 to 45 deg. The computed aerodynamic coefficients of each spike-tipped body are then examined, and the benefits are discussed afterward.

0-Degree AOA

Figure 7 is the interferogram of the flowfield around the disk-spike model for 0-deg AOA. The bow shock and the detachment zone in front of the nose model can be clearly recognized by light intensity differences on the interferogram. Remember, the light intensity distribution give integral information on the density gradient field in the gas flow.

Figure 8 shows the computed isobars in the plane of symmetry obtained by numerical simulation for conditions corresponding to the earlier experiment. The experimental and numerical results do not give the same physical quantity; however, the comparison is nevertheless possible. The visualized flow structure is accurately predicted by the CFD code except behind the disk, where the flow separates prematurely.

Figure 9a presents four interferograms of the flowfield around the sphere-spike model for 0-deg AOA. The consecutive pictures are extracted from a series of eight, obtained during a test: Two flow regimes are clearly highlighted. The transient flow regime, visible on the two first pictures from the left, starts immediately after the diaphragm bursts. The established flow regime is visible on the other two pictures and remains up to the end of the test.

Previous experiments[31] did not reveal these two flow regimes. Recent experiments[32] seem to show that for all spikes the flow structure is very sensitive to the flight conditions and to the spike length.

Figure 9b is an enlarged view of the last picture of Fig. 9a, which is comparable to the numerical simulation.

Figure 10 shows the computed isobars in the plane of symmetry obtained by numerical simulation for conditions corresponding to the earlier experiment. The visualized flow structure of the established flow regime is accurately predicted by the CFD code.

Figure 11 shows the interferogram of the flowfield around the biconical-spike model for the same angle of attack.

Figure 12 also shows the computed isobars in the plane of symmetry obtained by numerical simulation for conditions corresponding to the earlier experiment. The visualized flow structure is correctly reproduced by the computation.

When the results obtained for the three spikes are compared, it can be seen that the angles of the shock in front of the disk spike, the sphere spike, and the biconical spike are quite similar. However,

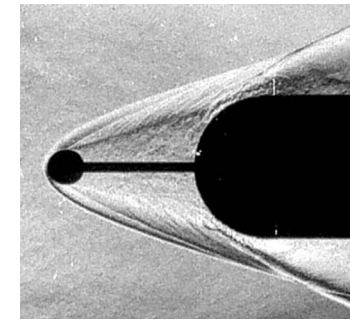

Fig. 9b DI for the sphere-spike model, $\alpha = 0$ deg, second flow regime.

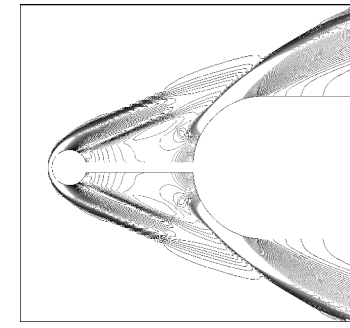

Fig. 10 Computed isobars for the sphere-spike model, $\alpha = 0$ deg.

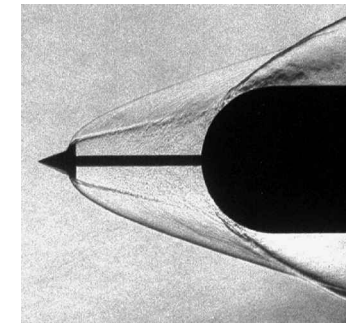

Fig. 11 DI for the biconicalspike model, $\alpha = 0$ deg.

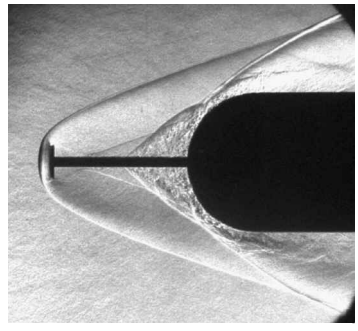

Fig. 7 DI for the disk-spike model, $\alpha = 0$ deg.

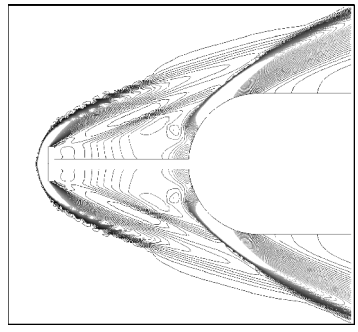

Fig. 8 Computed isobars for the disk-spike model, $\alpha = 0$ deg.

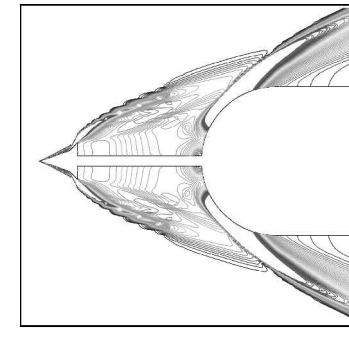

Fig. 12 Computed isobars for the biconical-spike model, $\alpha = 0$ deg.

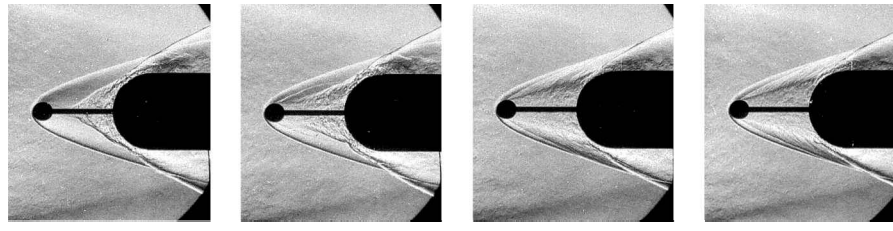

Fig. 9a DI for the sphere-spike model, $\alpha = 0$ deg, two flow regimes.

the distance between the shock and the body shoulder is shorter for the sphere spike and the biconical spike than for the disk spike.

The computation has the advantage of giving a quantitative insight into the flowfield. Thus, a higher pressure is found in cases of the sphere-spike and the biconical-spike models in the dome–nose region near the sting and in the shoulder region.

Figure 13 shows the comparison between the measured pressure coefficient distributions (symbols) on the forebody nose and the computed ones (solid lines). The blunt body, the disk-spike, and the sphere-spike models are studied. The results for the biconical spike are not available for the moment. Pretty good agreement is found: It is clear that the blunt-body pressure is much higher than that of the spike models. As a consequence, the drag of the blunt body is much higher than that of the spike models. The pressure on the sphere-spike model is slightly higher than that on the disk-spike model. This tendency is reproduced by the computation.

α = 16 and 20 Deg

Figure 14 shows the comparison of the numerical results for the spike-tipped models in the case of an angle of attack of 16 deg. The pressure on the models is represented by isolines. The major differences in the pressure distributions appear on the leeward side of the forebody noses, just above the spike sting.

Figure 15 presents the comparison between the measured pressure coefficient distributions on the domes and the computed distributions for the 16-deg AOA. Distributions on the windward, the middle (lateral), and the leeward sides are shown. The computation gives a good prediction of the pressure on the forebody surface, except near the nose of the forebody ($X \approx 70$ mm) in the stagnation region. At this location, the pressure gradient is very important, and the node distribution on the forebody surface should probably be refined. The flow in the stagnation region should also be better predicted by using another turbulence model to obtain a better agreement. However, the computation respects the experimental tendency.

Figure 16 shows the same kind of comparison between measurements and computations for the angle of attack of 20 deg: Again, the agreement is good.

α = 24 Deg

Figures 17 and 18 show the same kind of experimental images as Figs. 7 and 9b under the same flow conditions for an AOA of 24 deg. The flow pattern is different in the two cases. Differences can be clearly seen in the bow shock wave in front of the spike and near the center of the hemispherical forebody. The detachment of the flow at the sphere spike is less abrupt than the one at the classical disk spike. The flow structures A identified on the leeward side near the model domes are the result of the density gradient integration of the three-dimensional shock surrounding the domes.

Figures 19 and 20 show the same kind of computed results as Figs. 8 and 10, which correspond to the earlier experiments. Again, the CFD code predicts quite well the experimental flow structure. The three-dimensional flow structures A found in the experiments are not visible because Figs. 19 and 20 show the computed isobars in the symmetry plane. A higher pressure is found in the blunt nose region on the leeward side for the disk-spike model than for the sphere-spike model.

Figure 21 presents the comparison between the measured pressure coefficient distributions on the forebodies and the computed

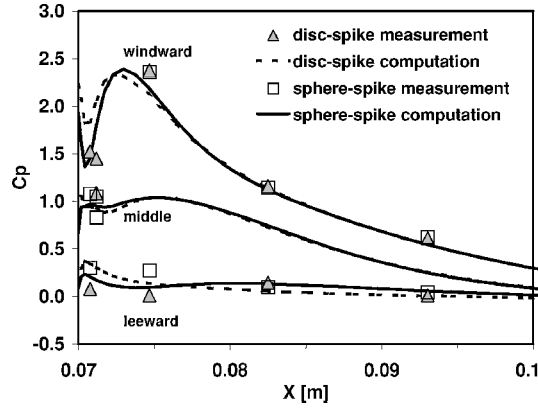

Fig. 15 Measured and computed pressure coefficients on the forebody, α = 16 deg.

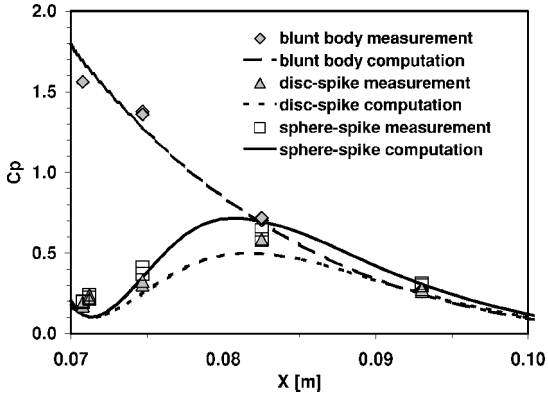

Fig. 13 Measured and computed pressure coefficients on the forebody, α = 0 deg.

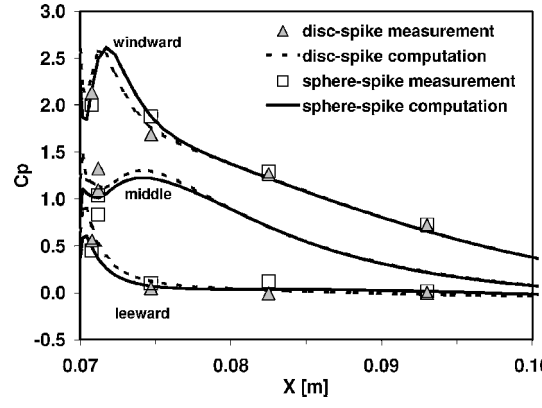

Fig. 16 Measured and computed pressure coefficients on the forebody, α = 20 deg.

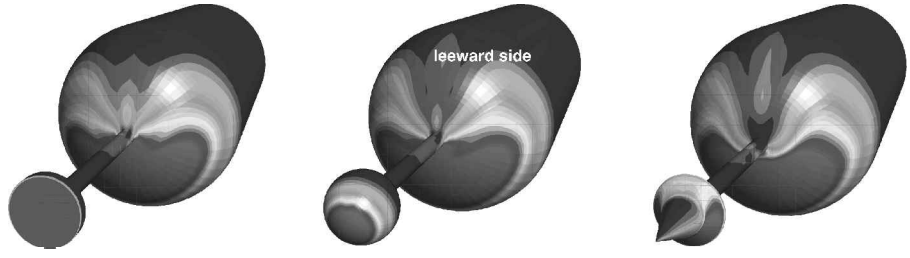

Fig. 14 Computed pressure for three spike-tipped models, α = 16 deg.

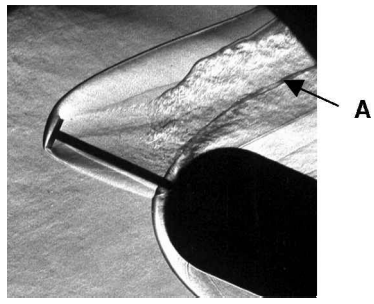

Fig. 17 DI for the disk-spike model, $\alpha = 24$ deg.

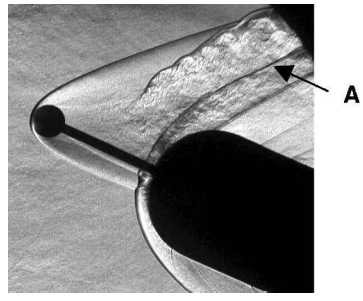

Fig. 18 DI for the sphere-spike model, $\alpha = 24$ deg.

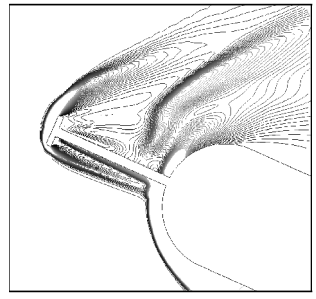

Fig. 19 Computed isobars for the disk-spike model, $\alpha = 24$ deg.

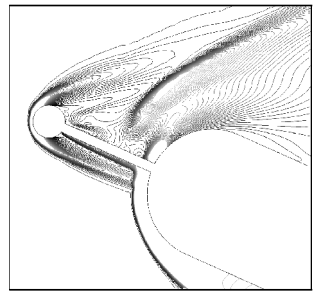

Fig. 20 Computed isobars for the sphere-spike model, $\alpha = 24$ deg.

distributions for the 24-deg AOA. Once more, the CFD code reproduces the pressure distribution on the forebody, except near the stagnation zone, where slight discrepancies exist.

When the pressure distributions for the presented AOA (Figs. 15, 16, and 21) are examined, the main differences between the models are located from the forebody nose ($X = 70$ mm) up to around 6 mm along the model axis ($X \approx 76$ mm), corresponding to a cap area of about 68 deg of the forebody nose. The pressure rise at the dome shoulder characterizes the flow reattachment. In the case of the sphere spike, it lags behind the one obtained in the case of the disk spike, and consequently, the sphere-spike drag will be smaller than that of the disk spike.

$\alpha = 30$ and 45 Deg

Figures 22 and 23 show the comparison of the numerical results for the spike-tipped models in the case of AOA of 30 and 45 deg, respectively. The pressure on the models is represented by isolines. For the 30-deg AOA, the major differences in the pressure distributions appear on the leeward side of the forebodies, just above the spike sting. For the 45-deg AOA, the pressure distributions on the forebodies are quite similar, indicating a quite similar drag.

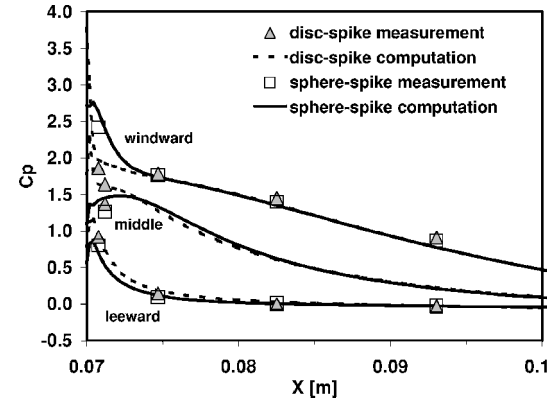

Fig. 21 Measured and computed pressure coefficients on the forebody, $\alpha = 24$ deg.

Aerodynamic Coefficients, Spike Benefits

The computations allow one to determine the global aerodynamic forces and moments, such as the drag, the lift, and the pitching moment. These results are presented to discuss the benefits of each spike-tipped geometry.

Figure 24 shows the spike contribution to the drag reduction: $(C_{d_{\text{hemis}}} - C_{d_{\text{spike}}})/C_{d_{\text{hemis}}}$. $C_{d_{\text{hemis}}}$ is the blunt-body drag, and $C_{d_{\text{spike}}}$ is the drag of the model with a spike. The disk-spike drag reduction ranges from 0 to 15 deg AOA. The sphere spike reduces the drag from 0 up to 19 deg AOA, and the biconical spike reduces the drag up to 21 deg. For AOA smaller than 5 deg, a 30–50% drag reduction is found, and the disk spike is the most efficient. For $5 \leq \alpha \leq 20$ deg, the biconical spike and the sphere spike are more efficient than the disk spike. Despite that the spike is penalizing for angles of attack greater than 21 deg, the biconical spike and the sphere spike are better than the disk spike for $20 \leq \alpha \leq 35$ deg. An increase in the drag of about 5% is found for $35 \leq \alpha \leq 45$ deg for all spikes.

Figure 25 presents the spike influence on the lift increase: $(C_{l_{\text{spike}}} - C_{l_{\text{hemis}}})/C_{l_{\text{hemis}}}$. $C_{l_{\text{hemis}}}$ is the blunt-body lift, and $C_{l_{\text{spike}}}$ is the lift of the model with a spike. This formula is used although it is undefined for 0-deg AOA: In fact, the lift coefficient goes to zero in all studied cases at this AOA. The disk-spike efficiency ranges from 0 to 25 deg AOA. The sphere spike and the biconical spike increase the lift up to 30 and up to 35 deg, respectively. The sphere spike and the biconical spike are more efficient than the disk spike up to 35 deg. There is a reduction of about 5% for $35 \leq \alpha \leq 45$ deg for all spikes.

Figure 26 combines the earlier results by showing the lift over drag increase, which is calculated by $(C_l/C_{d_{\text{spike}}} - C_l/C_{d_{\text{hemis}}})/C_l/C_{d_{\text{hemis}}}$. Again, this formula is deliberately used for the lift-to-drag ratio of the blunt body and the spike-tipped missiles; this quantity is presented although the formula is undefined for 0 deg AOA.

The use of the disk spike is only beneficial up to about 21 deg, whereas use of the sphere spike and use of the biconical spike are beneficial up to about 26- and 28-deg AOA, respectively.

Figure 27 shows the spike influence on the pitching moment increase: $(C_{m_{\text{spike}}} - C_{m_{\text{hemis}}})/C_{m_{\text{hemis}}}$. $C_{m_{\text{hemis}}}$ is the blunt-body pitching moment, and $C_{m_{\text{spike}}}$ is the pitching moment of the model with a spike. This formula is deliberately used, although it is undefined for 0-deg AOA. The moments are evaluated on the rotation axis at the base of the models.

An increase of the pitching moment is obtained for all spike geometries; however, the sphere spike is the most efficient, especially for AOA higher than 20 deg.

Figure 28 shows the center of pressure location for the hemisphere model and for the spike-tipped models. That location is determined from the forebody nose, and it is normalized by the model diameter. There are few modifications of the center of pressure location of the spike-tipped models compared to the model without a spike. The center of pressure moves backward with the AOA increase, which has a beneficial effect on the missile maneuverability.

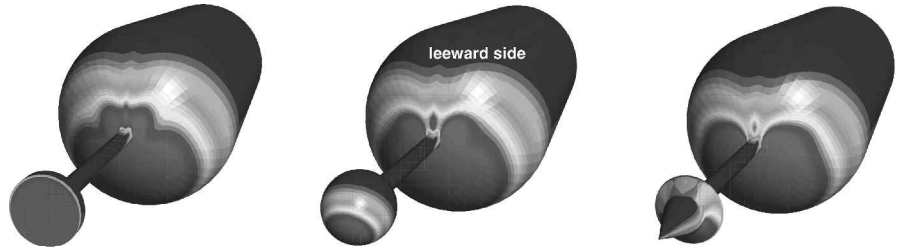

Fig. 22 Computed pressure for three spike-tipped models, $\alpha = 30$ deg.

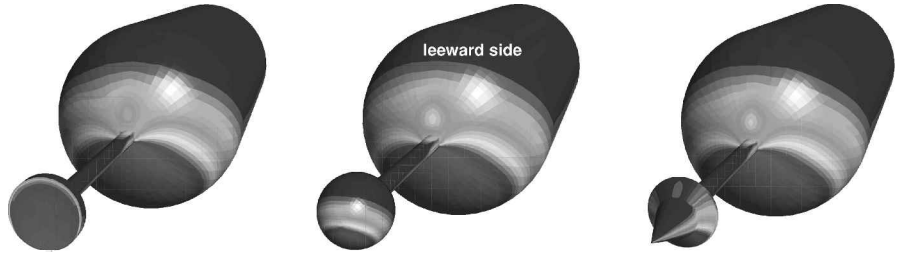

Fig. 23 Computed pressure for three spike-tipped models, $\alpha = 45$ deg.

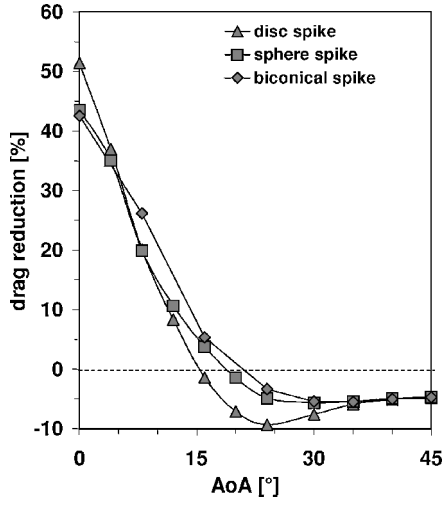

Fig. 24 Drag reduction for three spike-tipped models.

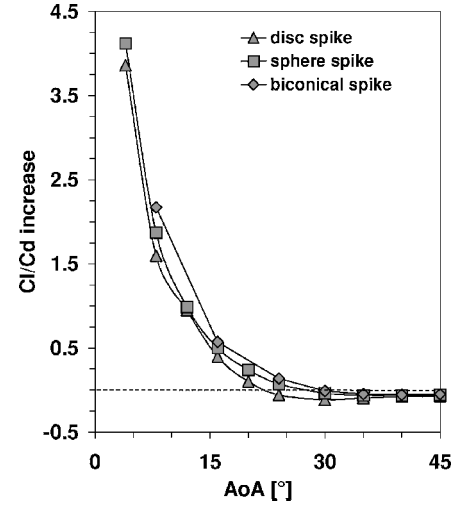

Fig. 26 Lift over drag increase for three spike-tipped models.

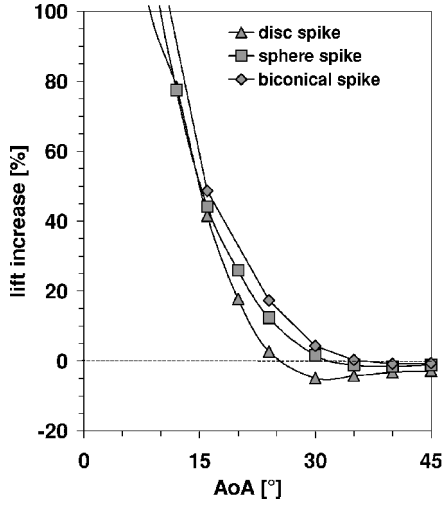

Fig. 25 Lift increase for three spike-tipped models.

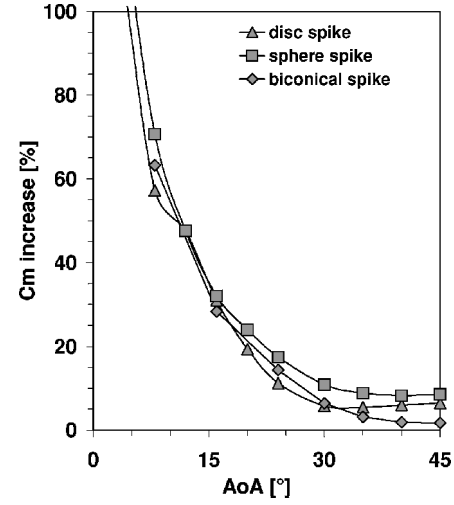

Fig. 27 Pitching moment increase for three spike-tipped models.

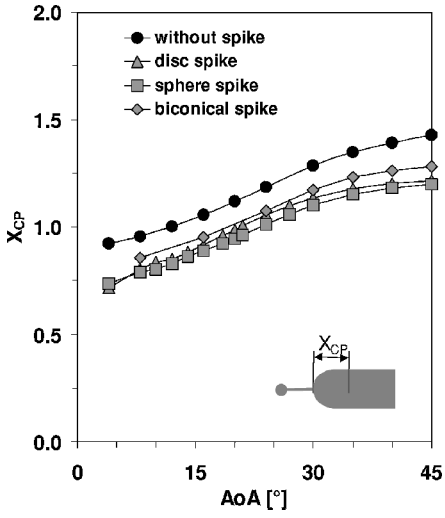

Fig. 28 Center of pressure for three spike-tipped models.

As a consequence of all the obtained results, missiles can be flown at higher AOA with the sphere spike and the biconical spike than with the disk spike.

Conclusions

Experimental investigations on disk-spike and sphere-spike missile models are successfully carried out at ISL using a shock tube as shock tunnel. Preliminary experimental investigations are also performed for a biconical-spike missile model. Interferograms are taken for flow visualization to study the flowfield around the spike-tipped bodies. Pressure measurements are also carried out on the nose of the dome models.

Steady-state numerical simulations of corresponding experiments are performed with a three-dimensional Navier–Stokes code to quantify the benefits obtained for each spike-tip geometry compared to the blunt body. The experimental and numerical investigations are carried out for a Mach number of 4.5 and for angles of attack ranging from 0 to 24 deg. The comparison of the computations with the experiments shows good agreement, especially for high AOA. However, agreement can probably be increased by using more refined meshes in the stagnation region and by using a more accurate turbulence model to better predict the separation.

Numerical investigations are also performed for the disk spike, the sphere spike, and a biconical spike for very high AOA ($\alpha \leq 45$ deg). Computations highlight a drag reduction from 0 up to 15, 19, and 21 deg for the disk spike, the sphere spike, and the biconical spike, respectively, compared to the blunt nose missile. The lift over drag ratio is significantly increased up to 21, 26, and 28 deg with the use of the disk spike, the sphere spike, and the biconical spike, respectively. The pitching moment is increased for all spikes and for all AOA. There are few changes in the position of the center of pressure of the spike-tipped missiles compared to the blunt nose missile. The center of pressure moves backward with the AOA increase for all missiles, which is beneficial to their maneuverability. The superiority of the aerodynamic behavior of the sphere spike and of the biconical spike for high and very high AOA is, therefore, clearly evident.

Experimental and numerical investigations of the heat flux on the forebody noses, where optoelectronic sensors will be placed, are in progress. Experiments with the biconical-spike model will also continue.

Acknowledgment

We thank the German Ministry of Defense for supporting this work under Contract BMVg 760/A 0001/R 1701-17.

References

[1]Mair, W. A., "Experiments on Separation of Boundary Layers on Probes in Front of Blunt-Nosed Bodies in Supersonic Air-Stream," *Philosophical Magazine*, Ser. 7, Vol. 43, No. 342, 1952, pp. 695–716.

[2]Stalder, J. R., and Nielsen, H. V., "Heat Transfer from a Hemisphere-Cylinder Equipped with Flow-Separation Spikes," NACA TN 3287, Sept. 1954.

[3]Bogdonoff, S. M., and Vas, E. I., "Preliminary Investigations of Spiked Bodies at Hypersonic Speeds," *Journal of the Aeronautical Sciences*, Vol. 26, No. 2, 1959, pp. 65–74.

[4]Crawford, D. H., "Investigation of the Flow Over a Spiked-Nose Hemisphere-Cylinder at a Mach Number of 6.8," NASA TN-D118, Dec. 1959.

[5]Ericsson, L. E., and Reding, J. P., "Dynamics of Separated Flow Over Blunt Bodies," Lockheed Missiles and Space Co., Inc., Rept. LMSC-2-80-65-1, Sunnyvale, CA, 1965.

[6]Reding, J. P., Guenther, R. A., and Richer, B. J., "Unsteady Aerodynamic Considerations in the Design of Drag Reduction Spike," *Journal of Spacecraft*, Vol. 14, No. 1, 1977, pp. 54–60.

[7]Zorea, C., and Rom, J., "Effect of a Spike on the Drag and on the Aerodynamic Stability of Blunt Bodies in Supersonic Flow," *Journal of Spacecraft*, Vol. 7, No. 8, 1970, pp. 1017–1019.

[8]Chang, P. K., "Flow Separation on Thin Protruding Probes Placed in Front of Blunt Bodies at Supersonic/Hypersonic Speeds," *Separation of Flow*, 1st ed., Interdisciplinary and Advanced Topics in Science and Engineering, Vol. 3, Pergamon, Oxford, 1970, pp. 469–530.

[9]Schaffar, M., "État de l'Art Concernant les Travaux sur les Projectiles à Pointe et les Sujets Connexes/Sachstand der Arbeiten zu Geschossen mit Spike und damit zusammenhängenden Themen," French–German Research Inst. of Saint-Louis, ISL Rept. R 118/98, Saint Louis Cedex, France, July 1998.

[10]Huebner, L. D., Mitchell, A. M., and Boudreaux, E. J., "Experimental Results on the Feasibility of an Aerospike for Hypersonic Missiles," AIAA Paper 95-0737, Jan. 1995.

[11]Boudreaux, E. J., Krishnamurty, V. S., Mitchell, A. M., and Shyy, W., "Experiments and Analysis of an Aerospike Flow Environment for Protecting Infrared Missile Dome," *Research and Technology Organization, Meeting Proceedings 5*, Sorrento, Italy, 1998, p. 13-1–13-17.

[12]Krishnamurty, V. S., and Shyy, W., "Computational Analysis of Hypersonic Turbulent Flows over a Projectile with Aerospike," *AIAA Journal*, Vol. 36, No. 2, 1995, pp. 163–172.

[13]Srulijes, J., Runne, K., and Seiler, F., "Flow Visualization and Pressure Measurements on Spike-Tipped Bodies," AIAA Paper 2000-2520, 2000; also French–German Research Inst. of Saint-Louis, ISL Rept. PU 349/2000, Saint Louis Cedex, France, Aug. 2000.

[14]Srulijes, J., Gnemmi, P., Runne, K., and Seiler, F., "Flow Visualization, Pressure Measurements and Numerical Calculations on Spike-Tipped Bodies," STAB-Symposium, Nov. 2000; also French–German Research Inst. of Saint-Louis, ISL Rept. PU 351/2000, Saint Louis Cedex, France, Nov. 2000.

[15]Patz, G., "Das Hyperschallstossrohrlabor des ISL, 3. Teil: Stossrohr B," French–German Research Inst. of Saint-Louis, ISL Rept. N 30/70, Saint Louis Cedex, France, Sept. 1970.

[16]Patz, G.,"Das Hyperschallstossrohrlabor des ISL, 2. Teil: Stossrohr A," French–German Research Inst. of Saint-Louis, ISL Rept. N 27/71, Saint Louis Cedex, France, Nov. 1971.

[17]Oertel, H., *Stossrohre*, Springer-Verlag, Vienna, 1966.

[18]Shoemaker, J. M., "Aerodynamic Spike Flowfields Computed to Select Optimum Configuration at Mach 2.5 with Experimental Validation," AIAA Paper 90-0414, Jan. 1990.

[19]Smeets, G., "Interferometry," French–German Research Inst. of Saint-Louis, ISL Rept. CO 214/90, Saint Louis Cedex, France, May 1990.

[20]CFX-TASCflow Computational Fluid Dynamics Software, Ver. 2.10, AEA Technology Engineering Software, Waterloo, ON, Canada, 2000.

[21]Cebeci, T., and Smith, A. M. O., "Analysis of Turbulent Boundary Layers," *Applied Mathematics and Mechanics 15*, Academic Press, New York, 1974.

[22]Launder, B. E., and Spalding, D. B., "The Numerical Computation of Turbulent Flows," *Computer Methods in Applied Mechanics and Engineering*, Vol. 3, No. 2, 1974, pp. 269–289.

[23]Huang, P. G., Bradshaw, P., Coakley, T. J., "Skin Friction and Velocity Profile Family for Compressible Turbulent Boundary Layer," *AIAA Journal*, Vol. 31, No. 9, 1993, pp. 1600–1604.

[24]Gnemmi, P., "Influence des Modèles de Turbulence sur la Prévision de l'Aérothermodynamique d'un Projectile de 155 mm," French–German Research Inst. of Saint-Louis, ISL Rept. CR/RV 458/2002, Saint Louis Cedex, France, July 2002.

[25]Gnemmi, P., "Influence des Modèles de Turbulence sur la Prévision de l'Aérothermodynamique de l'Avant-Corps d'Engins Génériques d'un Missile," French–German Research Inst. of Saint-Louis, ISL Rept. CR/RV 475/2002, Saint Louis Cedex, France, Sept. 2002.

[26]Yakhot, V., Orszag, S. A., Tangham, S., Gatski, T. B., and Speziale, C. G., "Development of Turbulence Models for Shear Flows by a Double Expansion Technique," *Physics of Fluids*, Vol. 4, No. 7, 1992, pp. 1510–1520.

[27]Grotjans, H., and Menter, F. R., "Wall Functions for General Application CFD Codes," *Computational Fluids Dynamics '98*, edited by K. D. Papailiou, Vol. 1, Pt. 2, Wiley, Chichester, England, U.K., 1998, pp. 1112–1117.

[28]Menter, F. R., "Two-Equation Eddy-Viscosity Turbulence Models for Engineering Application," *AIAA Journal*, Vol. 32, No. 8, 1994, pp. 1598–1605.

[29]Launder, B. E., Reece, G. J., and Rodi, W., "Progress in the Development of a Reynolds-Stress Turbulence Closure," *Journal of Fluid Mechanics*, Vol. 68, Pt. 3, April 1975, pp. 537–566.

[30]Speziale, C. G., Sarkar, S., and Gatski, T. B., "Modeling the Pressure–Strain Correlation of Turbulence: An Invariant Dynamical Systems Approach," *Journal of Fluid Mechanics*, Vol. 227, June 1991, pp. 245–272.

[31]Gnemmi, P., Srulijes, J., Roussel, K., and Runne, K, "Flowfield Around Spike-Tipped Bodies," AIAA Paper 2001-2464; also French–German Research Inst. of Saint-Louis, ISL Rept. PU 623/2001, Saint Louis Cedex, France, June 2001.

[32]Srulijes, J., Gnemmi, P., Seiler, F., and Runne, K., "Shock Tunnel High-Speed Photography and CFD Calculations on Spike-Tipped Bodies," French–German Research Inst. of Saint-Louis, ISL Rept. PU 649/2002, Saint Louis Cedex, France, Sept.–Oct. 2002.

R. M. Cummings
Associate Editor